Influence of the octahedral cation on the evolution of lattice phonons in metal halide double perovskites: Raman spectroscopic investigation of $Cs_2B'B''Cl_6$ ($B' = Ag_{1-x}Na_x$; $B'' = Bi_{1-x}In_x$)

Athrey C. Dakshinamurthy and C. Sudakar*
Multifunctional Materials Laboratory, Department of Physics, Indian Institute of Technology Madras, Chennai-600036, India

(Received 21 January 2023; revised 3 April 2023; accepted 15 May 2023; published 2 June 2023)

Vibrational dynamics in halide double perovskites govern several key aspects including carrier recombination and transport properties. Here, we present comprehensive vibrational studies investigated through micro-Raman spectroscopy to understand how octahedral cation substitution in a wide range of metal halide double perovskites $Cs_2B'B''Cl_6$ ($B' = Ag_{1-x}Na_x$; $B'' = Bi_{1-x}In_x$) influence lattice vibrations. A significant enhancement in F_{2g} mode intensity—a key factor in determining the cation ordering—is observed with Na^+ substitution. In contrast to a generally observed trend, despite similar ionic sizes of Na^+ and Bi^{3+}, an increase in cationic ordering is observed as Na^+ substitutes at Ag^+ site in $Cs_2Ag_{1-x}Na_xBiCl_6$ and $Cs_2Ag_{1-x}Na_xInCl_6$. The F_{2g} mode intensity depends on B'-site cationic ordering (Ag^+ or Na^+), while its vibrational energy is governed by the B''-site cations (Bi^{3+} or In^{3+}). The symmetric stretching vibrations depicted by A_{1g} mode are mainly influenced by [B^{3+}-X_6] octahedra. The reduction in the linewidth of symmetric-stretching LO phonon mode (A_{1g}) and the disappearance/diminishing of asymmetric-stretching vibrations (E_g) further substantiates the improved cationic ordering. The changes in the vibrational mode intensities with B'-site substitution (Ag^+, Na^+) and the appearance of distinct octahedral modes with B''-site substitution (Bi^{3+}, In^{3+}) allow us to disseminate different octahedral contributions to the vibrational dynamics in the lattice. Further, the vibrational analyses on double perovskites with different choices of B' and B'' cations and X anion reveal the origin of asymmetric stretching (E_g). This mode mainly prevails when sublattice distortions in the lattice exist. Thus, asymmetric-stretching mode can be a measure of sublattice distortion in the double perovskite, and a highly ordered system would exhibit very minimal or no asymmetric vibrations.

DOI: 10.1103/PhysRevMaterials.7.065401

I. INTRODUCTION

In the field of perovskite research, recent years have been largely devoted to exploring the strategies for enhancing the stability of metal halide perovskites and engineering the band gap for various applications [1,2]. Despite the exceptional optoelectronic properties of Pb-based perovskites, their wide acceptance for commercialization is impeded by two major challenges, viz., lead toxicity and long-term stability [3]. Significant efforts have been made to understand the superiority of lead halide perovskites and the fundamental origin of their unique optoelectronic properties, with an aim to discover compounds with similar functional properties [4,5]. Theoretical studies have shown that the ns^2 lone pair in Pb^{2+} and the high symmetry of the perovskite structure are major factors for the optoelectronic properties [5,6]. In this direction, cation transmutation with isoelectronic elements has been explored in the last few years to realize stable and lead-free perovskites without lowering the structural symmetry [7,8]. While the single-cation transmutation using Sn^{2+} or Ge^{2+} for Pb^{2+} does not lead to a stable structure due to the oxidation of cations, aliovalent substitution of a monovalent and a trivalent cation results in a high-symmetry cubic double-perovskite structure. Such structures with the general formula $A_2B'B''X_6$ exhibit exceptional stability owing to the octahedral coordination of B' and B'' atoms in a corner-sharing framework in three dimensions [9]. Various compositions for the choice of B' (Ag^+, Na^+, Cu^+), B'' (Bi^{3+}, In^{3+}, Sb^{3+}), and X (Cl^-, Br^-) have been realized while the A site is mostly occupied by inorganic Cs^+ or organic moieties (like MA, FA, BA, GA, etc.) [10].

All inorganic lead-free double perovskites have recently been employed for various optoelectronic applications including solar cells, light-emitting diodes, photodetectors, and x-ray imaging applications [9]. The device performance in all these applications is majorly governed by the carrier-phonon interactions in the crystal lattice [11,12]. Unlike the single perovskites, the lattice dynamics in the case of double perovskites are inherently complicated due to the dynamically vibrating two dissimilar interconnected octahedra in the sublattice. Strong exciton-phonon coupling necessitates understanding phonon dynamics and vibrational characteristics [13]. These will underpin various key features such as charge-carrier mobilities, thermal transport properties, and the excitonic emission aspects [14–16].

Raman spectroscopy has been the foremost choice among various spectroscopic techniques to unfold the vibrational characteristics of materials. Raman-scattering studies have been effectively used in the recent literature to understand the lattice vibrations [17], explore pressure and temperature phase diagrams [18–20], discern the degree of crystallinity, and monitor the stability and degradation aspects in halide

*csudakar@iitm.ac.in

perovskites [20,21]. Our earlier study on the vibrational characteristics of octahedra in $Cs_2Ag_{1-x}Na_xBiCl_6$ double perovskites reveals a strong influence of sublattice distortions on the band-gap engineering and excitonic emissions [22,23]. A strong synergy between the phonon vibrations with optical and electronic properties was thus unfolded [23]. Steele *et al.* have studied the intrinsic lattice phonon-scattering mechanisms to explain the interconnectedness of structural and electronic properties with vibrational attributes in $Cs_2AgBiBr_6$ [13]. Manna *et al.* have studied the lattice dynamics and Fröhlich interactions in $Cs_2AgIn_{1-x}Bi_xCl_6$ double-perovskite nanocrystals [16]. In a recent review by Spirito *et al.*, the potential of Raman-scattering studies to understand the phonon modes and correlate them to the optical and electronic properties in hybrid organic-inorganic layered perovskites has been discussed [24]. They also stress the need for further detailed Raman-scattering analysis in compositionally modified three-dimensional perovskites. While the compositional tuning in double perovskites has been a ready-to-go strategy to tailor various optoelectronic properties in halide double perovskites, understanding of the vibrational dynamics upon such compositional tuning is scarce for $Cs_2B'B''Cl_6$ double perovskites. The contributions of $B'X_6$ and $B''X_6$ octahedra to the phonon vibrations in these systems are also not clear in the literature. While cation ordering (B-site ordering) is well documented and is known to influence various physical or electronic properties in oxide perovskites [25–27], cationic ordering studies on halide perovskites are very meager.

In this paper we have systematically tailored the composition of $Cs_2B'B''Cl_6$ (with $B' = Ag_{1-x}Na_x$; and $B'' = Bi_{1-x}In_x$) double perovskites and studied the vibrational characteristics. Systematic changes in the vibration energies and the relative changes in the intensity of F_{2g}, E_g, and A_{1g} modes give the local structural details, including the cationic ordering, sublattice distortion, and octahedral concentration dependence on normal modes. This study unveils the different octahedral contributions to the vibrational dynamics in the lattice and the influence of B' and B'' cations in the octahedra on the structural ordering in these classes of compounds.

II. EXPERIMENT DETAILS

All the $Cs_2B'B''Cl_6$ (B' = Ag, Na; B'' = Bi, In) double perovskites are synthesized through the solution-precipitation method [22]. In a typical synthesis, 15 mL of HCl (36 wt. %) is taken in a beaker to which 2 mmol of precursor salt of B' [Ag(OAc) or NaCl] is added while the temperature is raised to 70 °C. The solution is stirred continuously till the salt dissolves completely, and then 2 mmol of precursor for B'' [$Bi(OAc)_3$ or $In(OAc)_3$] is added to the clear solution. The temperature of the solution is now raised to 135 °C and stirring is continued till the precursors are completely dissolved. Finally, 4 mmol of CsCl is added to the above clear solution, which immediately triggers the precipitation indicating the formation of a double-perovskite phase. After 30 min of continuous stirring, the solution is cooled naturally. The precipitate is filtered and washed with ethanol till the pH becomes neutral. The filtrate is dried overnight in a vacuum oven, and the product is ground into a fine powder and stored in a vial. Alloyed compositions of double perovskites, $Cs_2B'B''Cl_6$ (with $B' = Ag_{1-x}Na_x$; and $B'' = Bi_{1-x}In_x$; and x varying between 0 and 1), are synthesized through the same approach wherein a 2-mmol equivalent mixture of $(1-x)CH_3COOAg + xNaCl$ is used for $Cs_2Ag_{1-x}Na_xB''Cl_6$ (B'' = Bi or In), and 2-mmol equivalent mixture of $(1-x)Bi(CH_3COO)_3 + xIn(CH_3COO)_3$ is used for $Cs_2B'Bi_{1-x}In_xCl_6$ (B' = Ag or Na) synthesis.

A. Structural characterization

Powder x-ray-diffraction (XRD) studies on $Cs_2B'B''Cl_6$ compounds are performed in the 2θ range 10° to 70° with a step size of 0.01° using a Rigaku SmartLab powder x-ray diffractometer employed with a rotating anode Cu Kα ($\lambda = 1.5406$ Å) source operating at 4 kW. Room-temperature Raman spectra are acquired from a Horiba-Yvon (HR 800 UV) micro-Raman spectrometer with a He-Ne laser excitation source emitting photons of wavelength 632 nm with a laser power of ~5.02 mW. Power-dependent Raman spectra were also acquired on the double perovskites with the laser power ranging between 46 μW and 5.02 mW. Raman spectra are also acquired with an excitation laser of 488 and 532 nm. The spectral acquisition is carried out in a backscattered geometry with an Olympus microscope (100× objective lens) collecting the scattered radiation. The diffraction grating in the spectrometer is grooved with 1800 lines per millimeter. This gives a spectral resolution of less than 1 cm^{-1}. Further, the spectral parameters such as laser power, number of acquisitions, and acquisition time are kept constant for each set of samples. Compositional analyses have been carried out using FESEM energy-dispersive spectroscopy (EDS) (Inspect F50/Quanta 400) to estimate the actual composition of the compounds.

III. RESULTS AND DISCUSSION

A. X-ray-diffraction studies

X-ray diffraction (XRD) studies are performed to elucidate the phase purity and crystal structure information of $Cs_2B'B''Cl_6$ ($B' = Ag_{1-x}Na_x$; $B'' = Bi_{1-x}In_x$) double perovskites. Rietveld refinement is performed to extract the crystallographic parameters. The synthesized double perovskites are phase pure and devoid of any secondary phases, as evident from the high degree of crystallinity and absence of additional reflections from secondary phases. The synthesized double perovskites exhibit solid-solution behavior in bulk and crystallize into an elpasolite-type cubic polymorph with space-group $Fm\bar{3}m$ symmetry. A schematic representation of the double-perovskite crystal structure is shown in Fig. 1(a). The compounds exhibit a rocksalt ordering in the crystal, as inferred from all odd Miller indices in the XRD patterns. Such an ordering in perovskites is most preferred when the oxidation states of B' and B'' differ by greater than 2 [25,28]. While a charge difference of less than 2 mostly leads to a disordered rocksalt phase, a charge-valence difference of 2 would result in either an ordered or disordered rocksalt lattice [25,29]. Thus, in the present case, since the difference between the valence state of B' and B'' is 2, disordered, partially ordered, or fully ordered lattice can be observed, which is mainly governed by the charge state, size of cations occupying

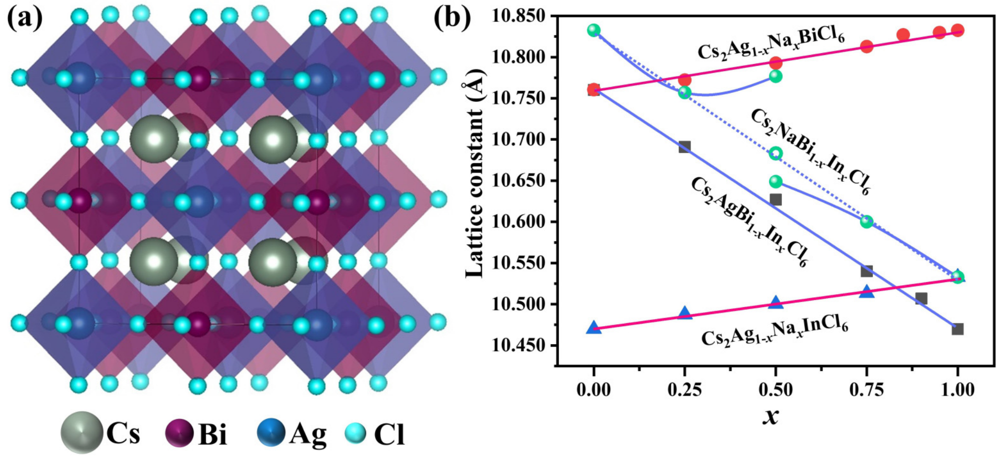

FIG. 1. (a) Crystal structure of $Cs_2B'B''Cl_6$ double perovskite. (b) Variation of lattice constant with composition in $Cs_2B'B''Cl_6$ double perovskites ($B' = Ag_{1-x}Na_x$ with $B'' =$ Bi or In; $B'' = Bi_{1-x}In_x$ with $B' =$ Ag or Na). Green open circle is the average lattice constant for $x = 0.5$ in $Cs_2NaBi_{1-x}In_xCl_6$ from phase fractions.

these sites, and the bonding preferences. The actual compositions of the synthesized samples have been estimated through energy-dispersive x-ray spectroscopy. All the compositions are indeed according to the nominal composition chosen for the compounds (i.e., $A : B' : B'' : X = 2 : 1 : 1 : 6$). Detailed compositional data and the corresponding EDS spectra for all the samples are given in the Supplemental Material (Table S1 and Fig. S2 in the Supplemental Material [30]).

The synthesized perovskite compounds are categorized into four series based on the choice of cation being substituted, viz., $Cs_2Ag_{1-x}Na_xBiCl_6$, $Cs_2Ag_{1-x}Na_xInCl_6$, $Cs_2AgBi_{1-x}In_xCl_6$, and $Cs_2NaBi_{1-x}In_xCl_6$. XRD studies on $Cs_2Ag_{1-x}Na_xBiCl_6$ series reveal that the lattice expands upon substituting Na^+ at Ag^+ site despite the former being smaller in size (1.02 Å) compared to the latter (1.15 Å). This is mainly due to the higher electronegativity of Ag (1.93) compared to Na (0.93). This leads to a large electronegativity difference between Na-Cl compared to Ag-Cl. Thus, the Ag–Cl bonds are mainly covalent in characteristics, while Na–Cl bonds are predominantly ionic. Rietveld refinement shows that the lattice constant varies linearly following Vegard's law from 10.7605 to 10.8326 Å for x varying between 0 and 1 in $Cs_2Ag_{1-x}Na_xBiCl_6$. Figure 1(b) shows the lattice constant variation with the compositional substitution for each series. The XRD patterns of all the synthesized double perovskites, and the refined XRD plot, are shown in Fig. 2.

The cationic ordering of B' (Ag^+ or Na^+) and B'' (Bi^{3+}) cations in the double-perovskite lattice can be inferred from the presence of a strong (111) diffraction peak in the XRD pattern [31,32]. These cations stack alternatively on (111) planes, and the extent of cationic ordering can be inferred directly from the intensity variation of these planes. With the increasing Na^+ substitution, the cationic ordering increases, as evident from the increase in the intensity of diffraction peaks for all odd (*hkl*). Also, the intensity ratio of diffraction planes (111) and (220) can be considered as a simpler way to assess such B'-B'' ordering in perovskites [33]. This ratio $[I_{(111)}/I_{(220)}]$ is found to be ~0.04 for $Cs_2AgBiCl_6$ ($x = 0$) and increases to ~0.34 for $Cs_2NaBiCl_6$ ($x = 1$). Such an improvement in the cationic ordering with Na^+ substitution is quite anomalous to the general trend for cationic ordering in perovskites [25,32]. A larger size mismatch between B' and B'' cations, in general, favors ordering. The lattice exhibits superior ordering in the present case when the size difference between B' and B'' cations is minimal. Figure 2(b) shows the XRD patterns of the $Cs_2Ag_{1-x}Na_xInCl_6$ series. The estimated lattice constant and unit-cell volume from the refined XRD data of $Cs_2Ag_{1-x}Na_xInCl_6$ also confirms the fact that Na^+ substitution results in lattice expansion while retaining the cubic structure. Even in this series, it is observed that the ratio $I_{(111)}/I_{(220)}$ is ~0.014 for $x = 0$ and gets enhanced to ~ 0.178 for $x = 1$; thus, B-site cationic ordering improves significantly with an increase in Na^+ substitution as evident from the enhanced (111) and other all-odd plane diffraction intensities. The pristine double perovskites are highly crystalline, and the XRD peak widths are in the same range ($2\theta \approx 0.09°$) as that of the standard samples used for crystallite size calibration, meaning that the broadening is only due to the instrumental factor and the crystallite sizes are much larger than 200 nm. It is observed that for the alloyed compositions, a slight increase in peak widths (~0.02° to 0.04°) is observed compared to both end members. A slight deviation from the actual composition can lead to such a broadening in the alloyed compositions.

The effect of trivalent cation ($B'' = Bi^{3+}$ and In^{3+}) substitution on the structure of $Cs_2B'B''Cl_6$ with fixed B' (Ag^+ or Na^+) is investigated by examining the XRD patterns of $Cs_2AgBi_{1-x}In_xCl_6$ and $Cs_2NaBi_{1-x}In_xCl_6$ compositions [Figs. 2(c) and 2(d)]. Figure 2(c) shows the refined XRD patterns of $Cs_2AgBi_{1-x}In_xCl_6$ wherein Bi^{3+} is being replaced with In^{3+}. All the XRD patterns correspond to the phase-pure cubic symmetry and are devoid of any phase segregations or secondary reflections from impurity phases. Rietveld refinement of XRD patterns of $Cs_2AgBi_{1-x}In_xCl_6$ [Figs. 1(b) and 2(c)] shows that $Cs_2AgBiCl_6$ lattice with lattice constant 10.7605 Å shrinks linearly to 10.4703 Å for $Cs_2AgInCl_6$ as the In^{3+} substitution increases. This is mainly due to the smaller ionic radii of In^{3+} (compared to Bi^{3+}) resulting in shorter bond lengths of In–Cl bonds compared to Bi–Cl bonds. Such lattice contraction is also evident from the shift of XRD reflections towards higher scattering angles with an

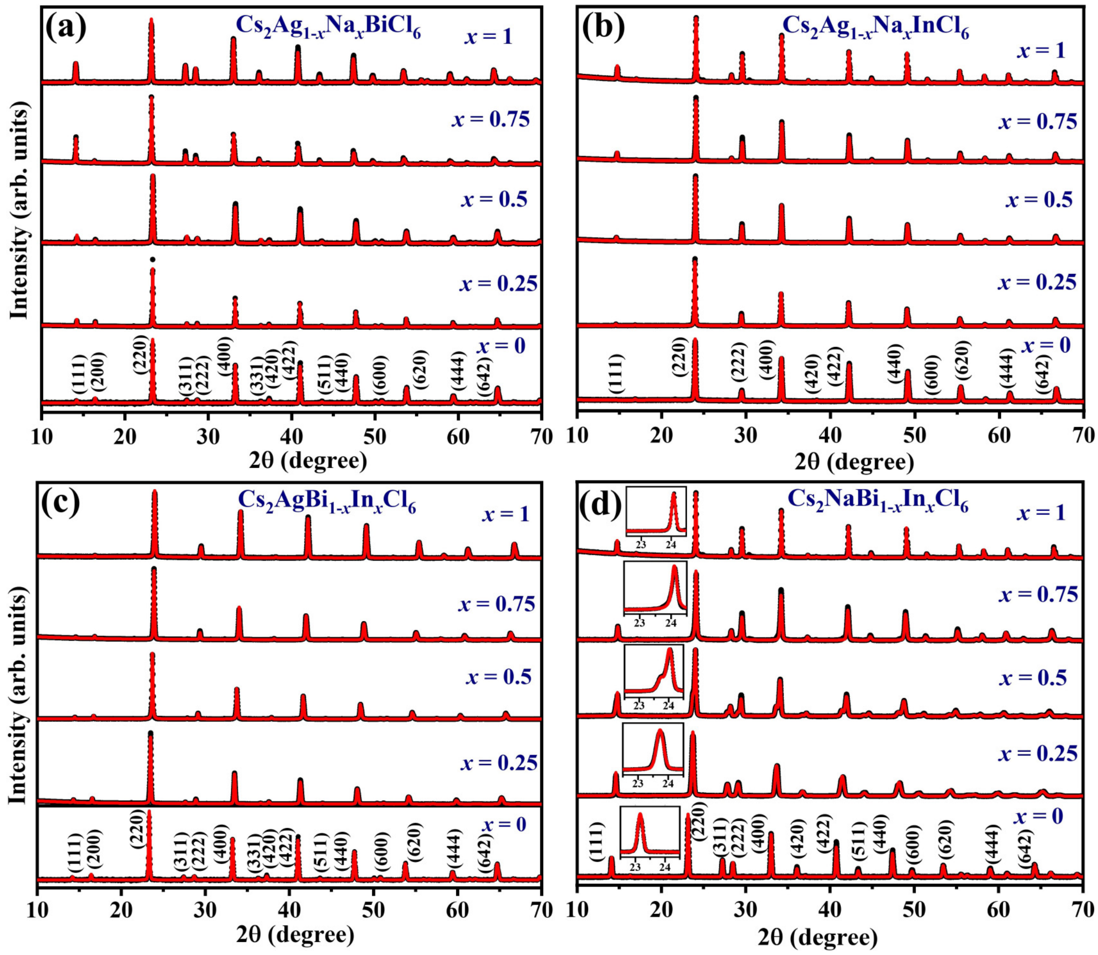

FIG. 2. XRD patterns and Rietveld refined plots for (a) $Cs_2Ag_{1-x}Na_xBiCl_6$, (b) $Cs_2Ag_{1-x}Na_xInCl_6$, (c) $Cs_2AgBi_{1-x}In_xCl_6$, and (d) $Cs_2NaBi_{1-x}In_xCl_6$ for $x = 0$ to 1. Also see Fig. S1 for raw XRD plots [30].

increase in In^{3+}. The results are the same even with the $Cs_2NaBi_{1-x}In_xCl_6$ series, wherein the In^{3+} incorporation at Bi^{3+} site tends to shrink the lattice. However, complete miscibility and phase purity are difficult to obtain for intermediate compositions of $Cs_2NaBi_{1-x}In_xCl_6$ [Fig. 2(d)]. For $x = 0.5$ in $Cs_2NaBi_{1-x}In_xCl_6$ we observe the XRD reflections have the signature of doublet peaks. This is very evident, especially at higher scattering angles. The doublet diffraction peaks are due to the presence of two cubic phases with different lattice parameters mostly from a mixture of compositions with $x < 0.25$ and $x > 0.75$ in $Cs_2NaBi_{1-x}In_xCl_6$. A strong tendency for the Bi and In atoms not to get miscible at B'' for $x = 0.5$ in $Cs_2NaBi_{1-x}In_xCl_6$, as also observed by Zhou *et al.* [34], is expected to be the cause for the mixed composite. They have investigated the effect of Bi^{3+} and In^{3+} transmutation on the structural and optical properties of $Cs_2NaBi_{1-x}In_xCl_6$ double perovskites. They also observed that complete solid solutions of $Cs_2NaBi_{1-x}In_xCl_6$ could hardly be obtained, and it was impossible to get phase-pure $Cs_2NaBi_{0.5}In_{0.5}Cl_6$ [34]. This can be understood in terms of formation energy for these compounds. The theoretically calculated formation energies per atom for $Cs_2NaBi_{1-x}In_xCl_6$ are positive, indicating that the solid solutions are less stable compared to their pristine end members. For $x = 0.5$, the formation energy per atom is estimated to be around 1 meV per atom, among the highest for $Cs_2NaBi_{1-x}In_xCl_6$ compounds [34]. High formation energy for $Cs_2NaBi_{0.5}In_{0.5}Cl_6$ makes it difficult to maintain the solid-solution behavior at $x = 0.5$ and hence drives the composition to take either Bi-rich or In-rich conditions. This suggests that the broad peaks with doublet signatures in the XRD patterns of $Cs_2NaBi_{0.5}In_{0.5}Cl_6$ could be due to a two-phase scenario. We performed refinement with the known crystallographic information details of compositions close to $x = 0.5$ and allowing the B'' occupancies to vary (Fig. S3 in the Supplemental Material [30]). A best fit for the diffraction pattern ($\chi^2 = 1.56$) was obtained for phase fraction of 73% for $Cs_2NaBi_{0.4}In_{0.6}Cl_6$ and 27% for $Cs_2NaBi_{0.78}In_{0.22}Cl_6$. It is noteworthy that the composition estimated using EDS analyses matches the nominal composition (Table S1 in the Supplemental Material [30].). It is interesting to note that the compositions estimated from the refinement also match with the extrapolated phase fraction estimated from Vegard's law (see Fig. S4 in the Supplemental Material [30]). In the lattice parameter vs x plot for the $Cs_2NaBi_{1-x}In_xCl_6$ we present lattice parameter values corresponding to both these phases. It is worthwhile to note that the average lattice parameter estimated based on the phase fraction obtained from the refinement is close to the

TABLE I. Wyckoff positions, corresponding site symmetries, and associated irreducible representations for the normal modes of vibrations in double perovskite.

$A_2B'B''X_6$ double perovskite (space group $Fm\bar{3}m$)				
Atom	Wyckoff position	Fractional coordinates	Site symmetry	Irreducible representation for the site symmetry
A	8c	(1/4,1/4,1/4)	T_d ($\bar{4}3m$)	$F_{1u} + F_{2g}$
B'	4a	(0, 0, 0)	O_h ($m\bar{3}m$)	F_{1u}
B''	4b	(1/2,1/2,1/2)	O_h ($m\bar{3}m$)	F_{1u}
X	24e	(1/4,0,0)	C_{4v} (4mm)	$A_{1g} + E_g + F_{1g} + 2F_{1u} + F_{2g} + F_{2u}$
$\Gamma_{total} = A_{1g}(R) + E_g(R) + 2F_{2g}(R) + F_{1g}(S) + 4F_{1u}(IR) + F_{2u}(S) + F_{1u}(ac)$				
Raman active: $2F_{2g} + E_g + A_{1g}$ (Four Raman-active modes)				

lattice parameter calculated from Vegard's law for $x = 0.5$ [Fig. 1(b) and Fig. S4 in the Supplemental Material [30]). It is evident that the lattice constant varies linearly with substitutional composition between the pristine end members (except for $Cs_2NaBi_{1-x}In_xCl_6$ near $x = 0.5$) following Vegard's rule suggesting a macroscopic solid-solution behavior. Further, a slight variation in the bond lengths of B'-X and B''-X upon substitution of B' or B'' cations is noted (Table S2 in the Supplemental Material [30]). Since the crystal structure remains in the cubic symmetry, the bond angles between B'–X–B'' are 180°. All three angles (α, β, γ) for the cubic structure remain 90° for all the compositions. The tolerance factors for halide double perovskites have been estimated and these values are found to be in the range of 0.9 to 0.96 for all the compositions (Table S3 in the Supplemental Material [30]).

B. Raman spectral studies

Despite the superiority in elucidating the crystal structure information of the compounds by diffraction methods such as XRD, the estimate is only an average from a large number of unit cells. On the other hand, spectroscopic techniques like Raman-scattering studies can probe the structural details down to the molecular scale, thereby revealing information that might differ from the global average [35]. Such local deviations, in addition to the atomic vibrations from their equilibrium positions in the crystal lattice, dictate various transport properties of the perovskites [36]. Further, the ordering of cations in the lattice plays a crucial role in dictating perovskites' electrical and optical properties [37,38]. To understand the local distortions by investigating the octahedral vibrations in these double perovskites and to underpin the cationic ordering in the lattice, Raman studies are performed on $Cs_2B'B''Cl_6$ double perovskites. Raman spectra of these double perovskites also confirm the phase purity and cubic system for these double-perovskite compounds. Any phase transition/distortion in the double-perovskite lattice would manifest itself with discernible changes in the Raman modes as these halide double perovskites are highly Raman active [39,40]. In fact, Raman spectroscopy has been extensively used to identify the distortions or symmetry lowering in double perovskites [40].

Group theory analysis on $Fm\bar{3}m$ space group provides an irreducible representation for Γ-point phonons as $\Gamma = A_{1g}(R) + E_g(R) + 2F_{2g}(R) + F_{1g}(S) + 4F_{1u}(\mathrm{IR}) + F_{2u}(S) + F_{1u}(ac)$ (Table I). The modes marked in the parenthesis R, IR, S, and ac refer to Raman active, infrared active, silent, and acoustic modes, respectively. Thus, four modes ($2F_{2g}$, E_g, A_{1g}) are Raman active in these double perovskites. These internal octahedral modes represent the bending (F_{2g}), asymmetric (E_g), and symmetric stretching (A_{1g}) of metal halide bonds in octahedra [22]. These vibrational modes are schematically shown in Fig. 3. Raman spectra of $Cs_2Ag_{1-x}Na_xBiCl_6$ and $Cs_2Ag_{1-x}Na_xBiCl_6$ compositions are presented in Fig. 4. The Raman modes from these phases are intense. The samples are very much stable under laser exposure without decomposing into other phases.

C. Influence of B'-site substitution

1. $Cs_2Ag_{1-x}Na_xBiCl_6$

The Raman spectra of the first series of compositions ($Cs_2Ag_{1-x}Na_xBiCl_6$), wherein the monovalent Ag^+ is being replaced with Na^+ at the B' site while the trivalent cation at B'' site is fixed with a Bi^{3+} cation, are shown in Fig. 4(a). The corresponding intensity contour plot is shown in Fig. 4(b).

It is evident from the spectra that Na^+ cation mixing at the Ag^+ site influences the octahedral vibrations in terms of vibrational frequencies and intensities. With the increase in Na^+ concentration at the Ag^+ site, the F_{2g} and A_{1g} modes show a minimal shift towards lower wave numbers, while the E_g mode exhibits a significant shift towards higher vibrational energies. This is mainly attributed to the expansion of octahedra with Na^+ substitution, as the Na–Cl bond length is longer than the Ag–Cl bond [41]. The intensity of the A_{1g} mode reduces with an increase in Na^+ concentration, while the F_{2g} mode intensity gets enhanced significantly. The intensity ratio

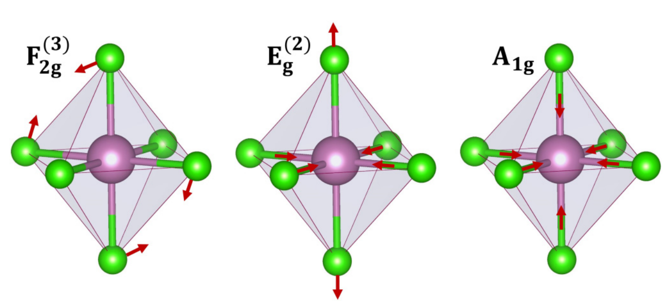

FIG. 3. Schematic representation of octahedral vibrational modes (superscript in the parentheses indicates degeneracy of the mode).

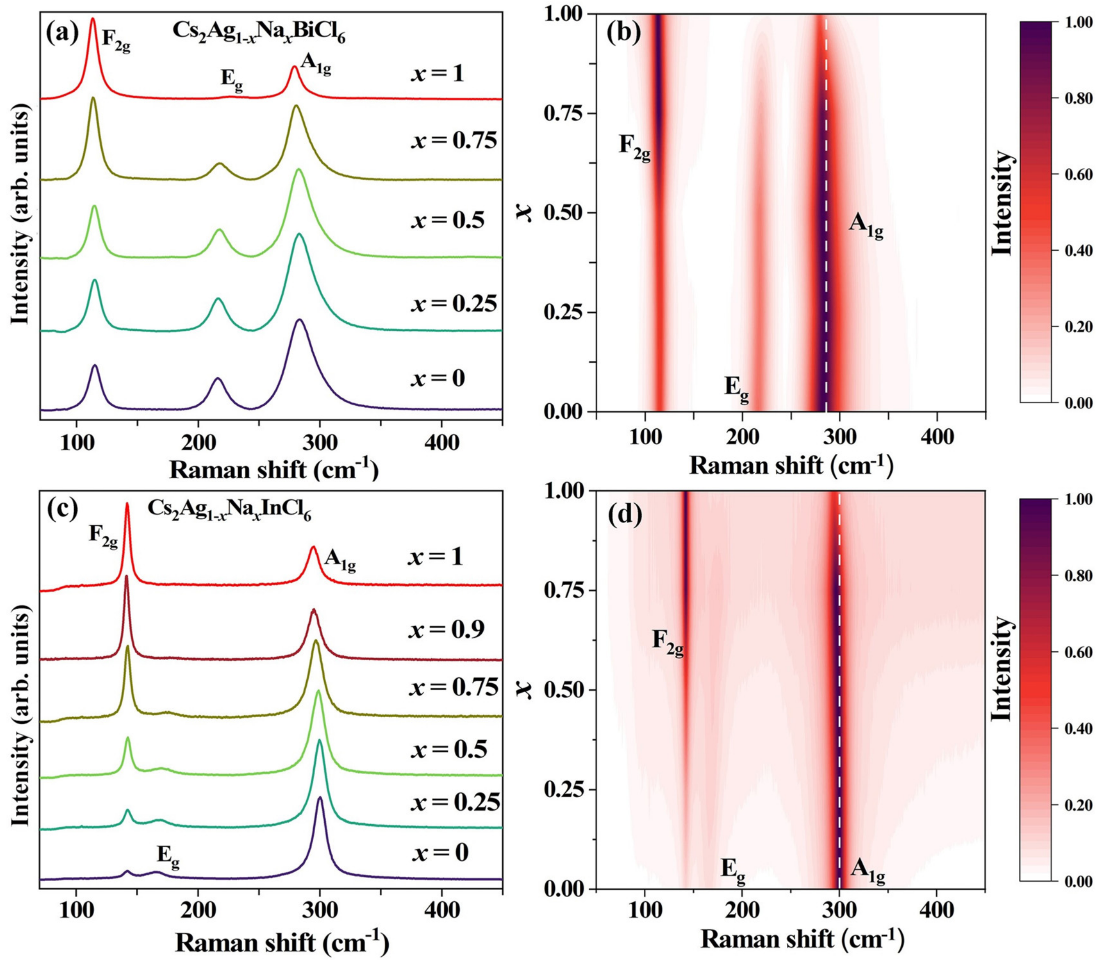

FIG. 4. Raman spectra of (a), (b) $Cs_2Ag_{1-x}Na_xBiCl_6$ (c), (d) $Cs_2Ag_{1-x}Na_xInCl_6$ for $x = 0$ to 1. (b) and (d) are intensity contour plots of (a) and (c).

among F_{2g}, E_g, and A_{1g} modes are further analyzed to investigate the sublattice distortion and the extent of ordering. Figure 5(a) shows the variation of integrated intensity ratio [$I(A_{1g})/I(F_{2g})$] with Na composition. This ratio $I(A_{1g})/I(F_{2g})$] is ∼4.6 for $x = 0$ and reduces to almost ten times, i.e., $I(A_{1g})/I(F_{2g})$] ∼0.46, for complete Na^+ replacement ($x = 1$). An increase in the intensity of F_{2g} mode has been attributed to improved crystal quality and cationic ordering in double perovskites, which is also in agreement with XRD studies, wherein the ordering increases with Na^+ substitution [31,41]. The asymmetric-stretching E_g mode becomes weak and almost disappears with complete Na^+ replacement at the Ag^+ site. Such a decrease in the intensity of E_g mode could be mainly attributed to the reduced sublattice distortions which arise out of octahedral mismatch. As one can see from the ionic radii differences, Na^+ (1.02 Å) and Bi^{3+} (1.03 Å) have nearly the same ionic radii, while Ag^+ is slightly bigger (1.15 Å). Thus, with an increase in Na^+ at the Ag^+ site, the mismatch between B' and Bi^{3+} reduces. The asymmetric stretching reduces, consequently, as evident from the disappearance of E_g mode in the Raman spectra.

Figure 5(b) shows the $I(F_{2g})/I(E_g)$ variation with x. The ratio increases to ∼26 (for $x = 1$) from near unity (for $x = 0$) as the double perovskite with $B' = Na^+$ system ($Cs_2NaBiCl_6$) exhibits very weak asymmetric-stretching vibrations. The influence of B'-cation substitution on the vibrational energies of $Cs_2Ag_{1-x}Na_xBiCl_6$ has been analyzed by plotting the variation of Raman mode positions as a function of substitution concentration (x) [Fig. 5(c)]. It is observed that the vibrational energies of F_{2g} mode show minimal change (∼1 cm^{-1}) while the A_{1g} modes tend to redshift with lowering of vibrational energies (5 cm^{-1}) upon increasing the Na^+ substitution. The A_{1g} mode, which is at ∼284 cm^{-1} for $x = 0$, decreases to ∼279 cm^{-1} for $x = 1$. Such a decrease is mainly attributed to the expansion of double-perovskite lattice resulting in the weakening of bond strengths, and thus the effective vibrational energies of symmetric-stretching vibrations decrease [41]. This is also evident from the increased bond lengths of Na–Cl compared to Ag–Cl bonds in $Cs_2Ag_{1-x}Na_xBiCl_6$ (Table S2 in the Supplemental Material [30]). The asymmetric-stretching E_g mode energies increase almost 12 cm^{-1} upon replacing Na^+ at the Ag^+ site. However, this mode gets significantly weaker with a feeble peak intensity upon completely substituting Na^+. This is due to increased cationic ordering and octahedral match with [$BiCl_6$] upon Na^+ substitution, as also evident from the XRD studies. Further, the full width at half maxima (FWHM) has been analyzed for these Raman modes and it was found

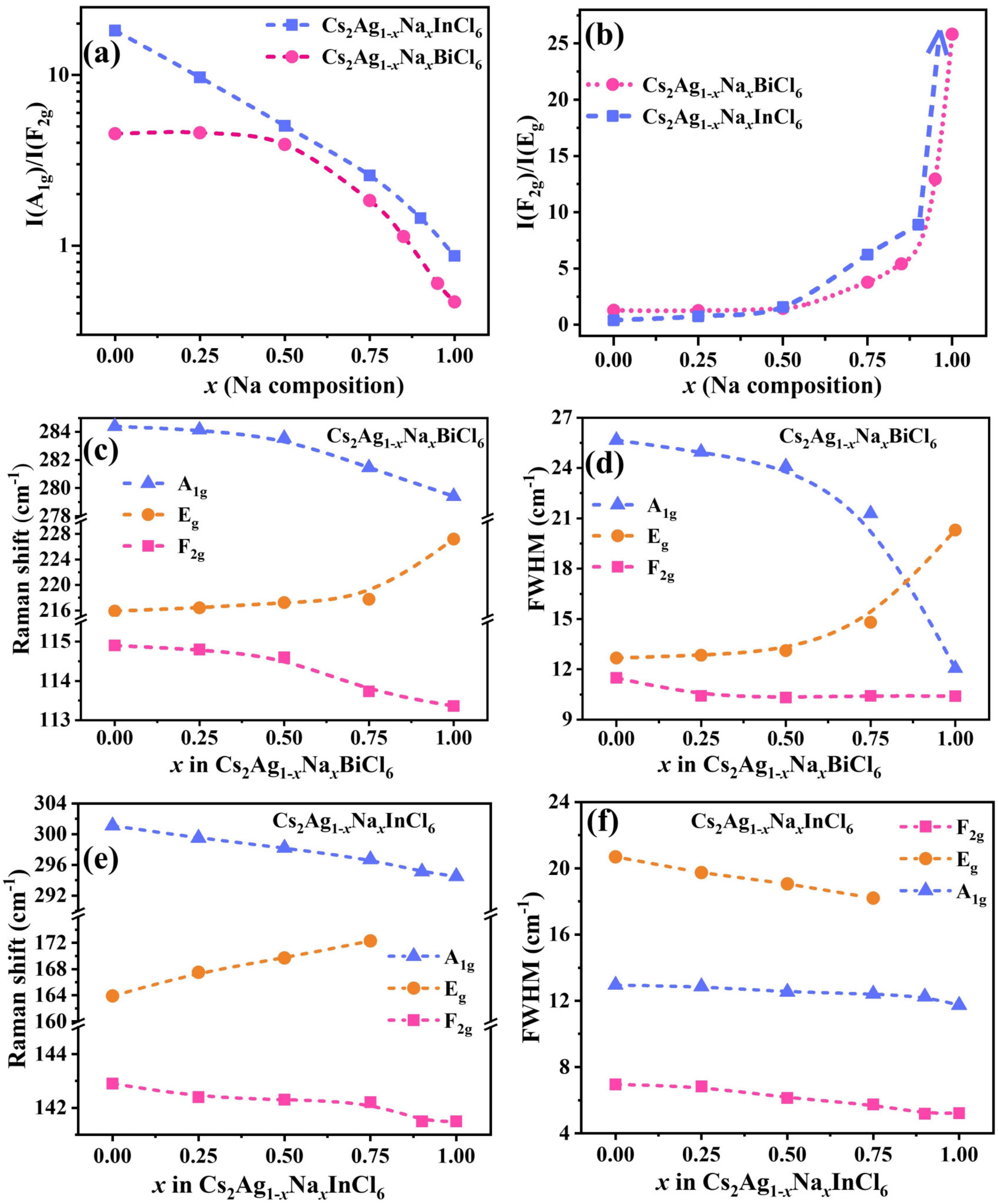

FIG. 5. Variation of integrated intensities (a) and (b), vibrational energies (c) and (e), FWHM (d) and (f) of Raman modes with Na composition in $Cs_2Ag_{1-x}Na_xBiCl_6$ and $Cs_2Ag_{1-x}Na_xInCl_6$.

that the width of A_{1g} mode reduces significantly upon Na^+ substitution at the B' (Ag^+) site [Fig. 5(d)]. The linewidth of A_{1g} mode which is $\sim 26\,\mathrm{cm}^{-1}$ (for $x = 0$) decreases to $\sim 12\,\mathrm{cm}^{-1}$ (for $x = 1$). It is also observed that the narrow A_{1g} mode in the case of $Cs_2NaBiCl_6$ becomes broad with a slight asymmetric profile for $Cs_2AgBiCl_6$, which is possibly due to increased anharmonicity owing to the lattice distortions or antisite defects [42]. The narrow values of FWHM of Raman modes with Na^+ replacement also indicate the fact that there is hardly any intermixing of B' and B'' atoms in the double-perovskite lattice [43]. The width of E_g Raman mode is observed to remain nearly the same till $x = 0.75$ and increases with complete substitution, although the peak itself almost disappears owing to reduced sublattice distortions. The low-frequency F_{2g} mode, which represents the translation of Cs atoms in the space surrounded by metal halide octahedra, could not be observed as it falls below the detectable range of the spectrometer used.

2. $Cs_2Ag_{1-x}Na_xInCl_6$

Figure 4(c) shows the Raman spectra of Na^+-substituted $Cs_2AgInCl_6$ double perovskites ($Cs_2Ag_{1-x}Na_xInCl_6$), and the corresponding intensity contour plots are shown in Fig. 4(d).

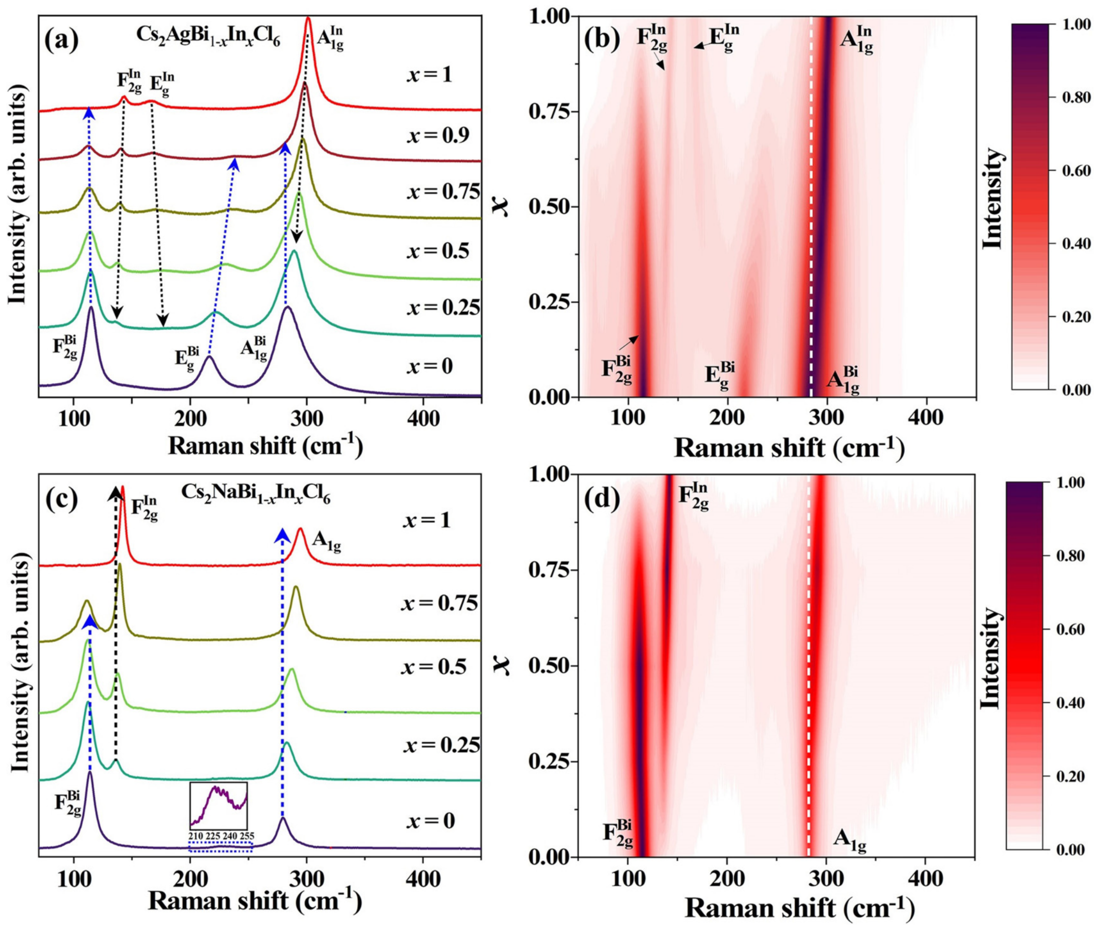

FIG. 6. Raman spectra of (a) $Cs_2AgBi_{1-x}In_xCl_6$ and (c) $Cs_2NaBi_{1-x}In_xCl_6$ for $x = 0$ to 1. (b) and (d) shows the corresponding contour maps.

The observations from the Raman spectra, in this case, are in concurrence with that made from the $Cs_2Ag_{1-x}Na_xBiCl_6$ compounds. Raman spectra of $Cs_2AgInCl_6$ (i.e., $x = 0$ in $Cs_2Ag_{1-x}Na_xInCl_6$) consist of three modes wherein the F_{2g} and E_g modes, which are close to each other, appear to be of low intensity in comparison to the intense A_{1g} mode. However, upon replacing the Ag^+ with Na^+ in $Cs_2AgInCl_6$, the intensity of F_{2g} mode increases significantly. This also suggests that the cationic ordering increases with Na^+ substitution. The integrated intensity ratio of $I(A_{1g})/(F_{2g})$ is ∼18.2 for $x = 0$, while it decreases to ∼0.87 for $x = 1$ in $Cs_2Ag_{1-x}Na_xInCl_6$ [Fig. 5(a)]. Further, $I(F_{2g})/I(E_g)$ ratio ∼0.4 for $x = 0$ increases significantly to ∼9 for $x = 0.9$, while the complete replacement of Na^+ ($x = 1$) leads to the disappearance of E_g mode; thus, $I(F_{2g})/I(E_g)$ ratio shoots up [Fig. 5(b)]. This is synchronous with the XRD results wherein the increased intensities of all-odd Miller indices are observed with increase in Na^+ content. Reduction in the distortion and increase in the cationic ordering is further strengthened by this fact. The asymmetric-stretching E_g mode diminishes with an increase in Na^+ and completely vanishes upon complete replacement of Na^+ at the Ag^+ site resulting in $Cs_2NaInCl_6$ composition. The observations on vibrational energies are consistent even for the $Cs_2Ag_{1-x}Na_xInCl_6$ series wherein a continuous decrease in the A_{1g} peak position (∼7 cm^{-1}) is observed upon replacing Na^+ at Ag^+ site [Fig. 5(e)]. On the other hand, the vibrational energies of F_{2g} modes are nearly identical. While the peak position of E_g mode increases almost ∼9 cm^{-1} till $x = 0.75$, its intensity significantly decays and the complete substitution of Na^+ leads to the disappearance of asymmetric-stretching vibrations. The change in peak width of Raman modes with Na^+ concentration is plotted in Fig. 5(f). The FWHM variation is nearly minimal (∼2 cm^{-1}) in the case of $Cs_2Ag_{1-x}Na_xInCl_6$ series while significant variation in intensities is evidenced.

Thus, it is clear from these spectral analyses that the asymmetric stretching in the octahedra (E_g), which is mainly Raman active when the sublattice distortions persist, gets significantly reduced upon replacing the Na^+ at the Ag^+ site, while the vibrational energies of octahedral modes are less affected by the monovalent cation substitution as the peak features remain the same.

D. Influence of B''-site substitution

1. $Cs_2AgBi_{1-x}In_xCl_6$

The effect of trivalent cation in the octahedra on the normal modes of vibrations is studied by modifying B'' cations. Specifically, Bi^{3+} is substituted with In^{3+} in the double perovskites by fixing the B' site with either Na^+ or Ag^+. Figure 6 shows the Raman spectra of $Cs_2AgBi_{1-x}In_xCl_6$ and $Cs_2NaBi_{1-x}In_xCl_6$ ($x = 0$ to 1) double perovskites.

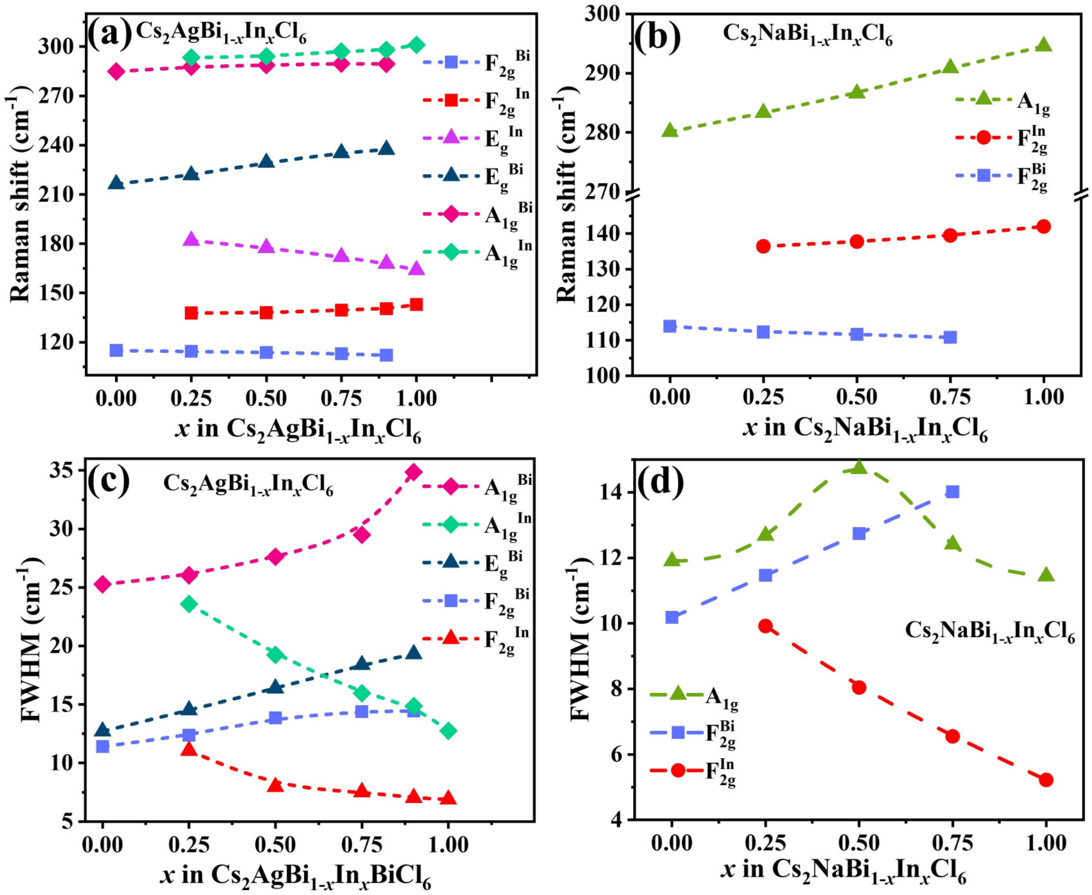

FIG. 7. Variation of vibrational energies (a) and (c) and FWHM (b) and (d) of Raman modes with In composition in $Cs_2AgBi_{1-x}In_xCl_6$ and $Cs_2NaBi_{1-x}In_xCl_6$.

Raman spectra of B''-substituted double perovskites show the following interesting features. First, with B'' cationic substitution, the presence of only octahedral modes corresponding to cubic double-perovskite crystal system confirmed that there is no symmetry lowering in crystal structures. Second, unlike the B' (Ag^+ or Na^+) substitution, wherein mainly the intensity variations in the normal modes of vibrations are observed, the B'' substitution results in the evolution of additional normal modes. These features can be clearly visualized through intensity contour plots shown in Figs. 6(b) and 6(d). These features reveal the distinct vibrational characteristics of $BiCl_6$ and $InCl_6$ octahedra. The vibrational characteristics of the octahedral framework get strongly impacted by the In^{3+} substitution at the Bi^{3+} site due to the largely differing ionic radii between Bi^{3+} ($r_{Bi} = 1.03$ Å) and In^{3+} ($r_{In} = 0.8$ Å) and high electronegative nature of Bi^{3+} compared to In^{3+}.

Figure 6(a) shows that the end members of $Cs_2AgBi_{1-x}In_xCl_6$, i.e., $Cs_2AgBiCl_6$ and $Cs_2AgInCl_6$, exhibit three distinct Raman modes corresponding to M-X_6 octahedra (F_{2g}, E_g, and A_{1g}) as discussed in the earlier section. For the in between mixed compositions, the Raman modes from both end members are present, with slightly modified vibrational energies. The Raman peak positions and the intensities evolve systematically with the compositional variation. For instance, $x = 0$ in $Cs_2AgBi_{1-x}In_xCl_6$ shows three modes of vibration at 114, 216, and 283 cm^{-1}. Upon increasing In^{3+} ($x = 0.25$), three additional vibrations modes are observed at 135, 178, and 277 cm^{-1} in addition to the Raman modes from $BiCl_6$ octahedra. These arise from the stretching and bending motions of [$InCl_6$] octahedra from the $Cs_2AgInCl_6$ structure. The Raman modes of mixed compounds highlight that these modes are predominant characteristics of B''-X_6 octahedra. The intensities of these modes are very much dependent on the mixing concentration. Even for a 10 at. % of Bi^{3+} substitution ($x = 0.9$), the distinct Raman modes from two different trivalent cation octahedra are seen. While the observation from XRD implies complete miscibility, the inference from Raman spectra shows that at the microscopic level, the Bi-X_6 and In-X_6 octahedra have distinct features. Thus, Raman spectral analyses have a unique advantage over the diffraction techniques, whereby the changes in the octahedral environment can be discerned directly. The intensities of F_{2g} modes are thus a direct indication of the population of B''-X_6 octahedra. With the increase in In^{3+} at the Bi^{3+} site, the intensity of modes corresponding to In-Cl_6 octahedra also increases while that of the Bi-Cl_6 octahedral vibrations decreases. This can be understood as the population of In-Cl_6 octahedra increases while Bi-Cl_6 decreases, thus resulting in corresponding intensity changes. The Raman spectra of these compositions have been deconvoluted, and the corresponding changes in the mode positions and the peak widths are analyzed (Fig. 7). The vibrational energy of F_{2g} mode from $BiCl_6$ octahedra remains mostly unaltered with change in In/Bi concentration, while the same mode from

$InCl_6$ octahedra shifts towards slightly higher vibrational energies (~8 cm^{-1}) [Fig. 7(a)]. We also observe changes in the vibrational energies of A_{1g} and E_g modes with In^{3+} substitution. The highly intense A_{1g} mode from $InCl_6$ octahedra shows a blueshift (~9 cm^{-1}) in vibrational energy with In^{3+} substitution due to increased force constants of In–Cl bonds. Shorter In–Cl bond lengths result in stiffer bonds and hence higher vibrational energies. The E_g mode from $[InCl_6]^{3-}$ octahedra in the pristine $Cs_2AgInCl_6$ compound slightly shifts (~16 cm^{-1}) towards lower wave numbers as Bi^{3+} concentration increases, while the same E_g mode from $[BiCl_6]^{3-}$ octahedra in the $Cs_2AgBiCl_6$ shifts (~22 cm^{-1}) towards higher wave numbers (refer to the dotted lines shown in Fig. 6). This is mainly ascribed to the elongation of In–Cl bonds at higher Bi^{3+} concentrations resulting in a smaller force constant in the In-Cl_6. On the other hand, with increasing In^{3+}, the Bi–Cl bonds shorten, and hence Bi-Cl_6 related E_g mode increases in energy. Due to the smaller size of In^{3+} and stronger In–Cl bonds, the $InCl_6$ octahedra experience compression. Thus, the connected $AgCl_6$ octahedra might experience expansive (isotropic tensile) chemical pressure [44]. This further leads to the compression in the Bi–Cl bonds in order to compensate for the pressure from the adjacent octahedra. The resulting increased stiffness in the Bi–Cl bonds can lead to a blueshift in the E_g mode of $BiCl_6$ with an increase in In^{3+} [44]. The variation in the peak widths of these Raman modes as a function of In^{3+} composition is shown in Fig. 7(c). The peak intensity of symmetric-stretching vibrations from ($BiCl_6$) octahedra (A_{1g}) diminishes gradually while its peak becomes broader and merges with the corresponding mode from $InCl_6$ octahedra due to an increase in the population of $InCl_6$ octahedral units in the In-rich composition. This is also evident from the narrow A_{1g} mode evolution from $InCl_6$ octahedra with In^{3+}. Thus, a clear compensatory increase (9 cm^{-1}) and decrease (11 cm^{-1}) of peak widths of A_{1g} modes from $BiCl_6$ and $InCl_6$ octahedra can be seen in $Cs_2AgBi_{1-x}In_xCl_6$. Similar behavior is observed even in the peak widths of F_{2g} modes from these two octahedra. The peak width of F_{2g} mode from $BiCl_6$ octahedra increases slightly while that of $InCl_6$ octahedra decreases nearly to the same extent (~3–4 cm^{-1}).

2. $Cs_2NaBi_{1-x}In_xCl_6$

The Raman mode characteristics of $Cs_2NaBi_{1-x}In_xCl_6$ ($x = 0$ to 1) are also in line with the $Cs_2AgBi_{1-x}In_xCl_6$ system [Figs. 6(c) and 6(d)]. The pristine compounds show two intense peaks one from bending (F_{2g}) and the other from the symmetric-stretching (A_{1g}) vibrations of M-X_6 octahedra. Unlike the spectral features in $Cs_2AgBi_{1-x}In_xCl_6$, the F_{2g} modes are intense for both the end members in $Cs_2NaBi_{1-x}In_xCl_6$. The asymmetric stretching (E_g) is very feeble for $x = 0$ and completely absent in the $x = 1$ compound. The intermediate compositions exhibit vibrational modes that arise from both $BiCl_6$ and $InCl_6$ octahedral vibrations. The compositional-dependent Raman spectra in Fig. 6 clearly show the emerging $[InCl_6]^{3-}$ and diminishing $[BiCl_6]^{3-}$ F_{2g} modes due to the increase in In^{3+} concentration in $Cs_2NaBi_{1-x}In_xCl_6$ ($x = 0$ to 1).

The intensity of the A_{1g} mode in $Cs_2NaBi_{1-x}In_xCl_6$ is relatively weak compared to the other series discussed in the previous section. Also, it remains mostly symmetric, thus considered as a contribution from both these octahedral units. The vibrational energies of F_{2g} modes are clearly distinct for these two octahedra in $Cs_2NaBi_{1-x}In_xCl_6$ and show a clear compositional dependence. The F_{2g} mode vibrations from $InCl_6$ octahedra become stiffer (~6 cm^{-1}) with an increase in In^{3+} concentration in the composition, and the corresponding mode from $BiCl_6$ octahedra gets slightly softer (3 cm^{-1}) [Fig. 7(b)]. The observations on FWHM values of these modes are also in line with the $Cs_2AgBi_{1-x}In_xCl_6$ case. The peak width of F_{2g} mode from $InCl_6$ octahedra decreases while F_{2g} mode from $BiCl_6$ octahedra broadens (~4 cm^{-1}) [Fig. 7(d)]. The FWHM of A_{1g} mode is narrow on either side of $x = 0.5$ and the composition with $Cs_2NaBi_{0.5}In_{0.5}Cl_6$ shows slightly broader A_{1g} features. This could be due to the convolution of two modes, as this particular composition is found to be a composite of two phases of Bi-rich and In-rich compositions from XRD analysis. Thus, although the competing nature of vibrations in adjacent octahedra prevails in a corner-connected framework, the influence of $[B^{3+}$-$X_6]^{3-}$ octahedra on lattice vibrations is significantly larger. Upon substitution with a B''-site cation which forms distinct octahedra, the spectra exhibits distinct vibrational energies. Thus, such vibrations can be discerned clearly in substituted double perovskites. It should be noted that these additional modes from substituted octahedra are still the same stretching and bending vibrations but just with different energies and should not be treated as arising from a tilting or distortion in the octahedra.

In general, due to the stronger bonding characteristics of B^{3+}-Cl_6 octahedra compared to B^{1+}-Cl_6 octahedra in $Cs_2B'B''Cl_6$, the Raman modes (F_{2g}, E_g, and A_{1g}) are mainly governed by the B^{3+}-X_6 octahedral units [39,45]. In the case of ordered $Fm\bar{3}m$ double perovskites, where well-defined corner-connected octahedral framework prevails, the observed Raman modes are expected to be a result of coupled vibrations of B'-X_6 and B''-X_6 octahedra [46]. However, the normal modes from the octahedra with stronger bonding characteristics become vibrationally significant, as proposed by Liegeois-Duyckaerts and Tarte in the virtual octahedral model [47]. In their work on Raman studies of $A_2B^{2+}B^{6+}O_6$ double perovskites with cubic symmetry, it is shown that $[B^{6+}$-$O_6]$ octahedral units are of significant vibrational importance due to the fact that the $[B^{6+}$-$O_6]$ octahedra are strongly bonded than the $[B^{2+}$-$O_6]$ octahedra. And thus, the observed Raman vibrational frequencies can approximately be described as the internal modes of vibration from an isolated $[B^{6+}$-$O_6]$ octahedron (virtual octahedra). Such consideration is well accepted by the scientific community, and it has been found to be the case in various other double-perovskite systems as well [39,45,48].

Even in the halide double perovskites, Elias *et al.* have recently shown that the vibrational modes in $Cs_2AgSbCl_6$ are mainly due to the vibrational response from $[SbCl_6]$ octahedral unit, since Sb–Cl are more strongly bonded as compared to Ag–Cl bonding in $[AgCl_6]$ octahedra. Silver ions contribution to the vibrational spectrum is meager due to their rigid displacements against chloride ions, similar to the case found in oxide double perovskite [45]. This has been supported through the density-functional theory analyses as well for $Cs_2AgSbCl_6$. Our detailed Raman studies on $Cs_2B'B''Cl_6$ are consistent with these observations. Upon changing the B' cation (Ag^+ or Na^+), we only observe intensity variations in the Raman modes with slight changes in their vibrational energies. However, alloying the B'' cation (with Bi^{3+} and In^{3+}) in the lattice leads to distinct octahedral modes. Bi/In–X bonds are much stronger compared to Ag–X bonds in $Cs_2AgBiCl_6$ and $Cs_2AgInCl_6$ [49]. Thus, [$BiCl_6$] or [$InCl_6$] internal octahedral modes become vibrationally significant and distinctly observed. Therefore, substituting the B'' cation with strong bonding characteristics with the Cl ion in the lattice result in two distinct sets of internal vibration modes from these two octahedral units ([$BiCl_6$] and [$InCl_6$]). These unequivocally explain the observation of two distinct sets of octahedral vibrational modes in substituted double perovskites. The change in concentration of B'' cations manifests as a systematic change in the intensity of octahedral modes. It should further be noted that the vibrational energies corresponding to F_{2g} and A_{1g} modes from [$InCl_6$] octahedra are larger compared to the respective modes from [$BiCl_6$] octahedra. This is mainly due to the fact that Bi^{3+} is much heavier compared to In^{3+}, thus resulting in lower vibrational energies based on harmonic oscillator approximation ($\omega = \sqrt{\frac{k}{\mu}}$).

We have also acquired the Raman spectra under different laser excitation energies and also under different laser intensities to check the influence of laser-induced effects, if any, on these Raman modes. These spectra are given in Fig. S5 and Fig. S6 in the Supplemental Material [30]. The spectra remain the same without any appearance of additional modes, thus ruling out the laser-induced effects or electron-phonon interactions. We would like to highlight here that the electron-phonon coupling in the double-perovskite lattice could only result in higher-order overtones of A_{1g} Raman modes which has been recently observed by Kai-Xuan *et al.* and Zhang *et al.* in halide double perovskites [50,51]. Thus, the origin of additional modes in the Raman spectra of intermediate compositions for B'' alloyed compounds is only due to two distinct sets of internal octahedral vibrations from [$BiCl_6$] and [$InCl_6$] octahedral units.

Since the octahedral arrangement and its contribution to vibrational dynamics is a key component for the observation of superior optoelectronic properties, introducing substituent to the lattice by trivalent doping/alloying can be very beneficial for enhancing emission properties [52]. One can find from recent studies that a small amount of trivalent metal cation doping in the alloyed double perovskites is shown to outperform in terms of their emission properties [53,54].

The local arrangement of cations in the lattice has been a subject of interest in the field of perovskites. Raman spectroscopy has been widely used in the literature as a complementary technique to XRD to discern the structural information including cationic ordering in the lattice since XRD alone has limitations due to differences in atomic-scattering factors of B-site cations. Generally, narrow and intense Raman modes are indicative of a well-ordered lattice, while the disordered systems exhibit broad peaks [42]. For instance, Runka *et al.* have proposed that the narrow and intense F_{2g} mode in the Raman spectra can be considered a key factor in determining the B-site order in perovskites [55]. Further, F_{2g} mode intensity is observed to be very much susceptible to changes in the B-site ordering, and its intensity is shown to decrease with a decrease in the degree of order. Reaney *et al.* also pointed out that the intensity of F_{2g} mode and linewidth of A_{1g} mode is a measure of the long-range ordering of cations [42]. Thus, our Raman spectral analyses on halide double perovskites, $Cs_2Ag_{1-x}Na_xBiCl_6$ and $Cs_2Ag_{1-x}Na_xInCl_6$, irrefutably demonstrate that the cationic ordering increases with Na^+ substitution at the Ag^+ site. Further, detailed compositional-dependent Raman spectral analyses on a series of double perovskites suggest that the F_{2g} mode intensity depends on B' cationic ordering (Ag^+ or Na^+) while its vibrational energy is governed by the B'' cations (Bi^{3+} or In^{3+}). The symmetric-stretching vibrations depicted by A_{1g} mode are mainly influenced by [B^{3+}-X_6] octahedra.

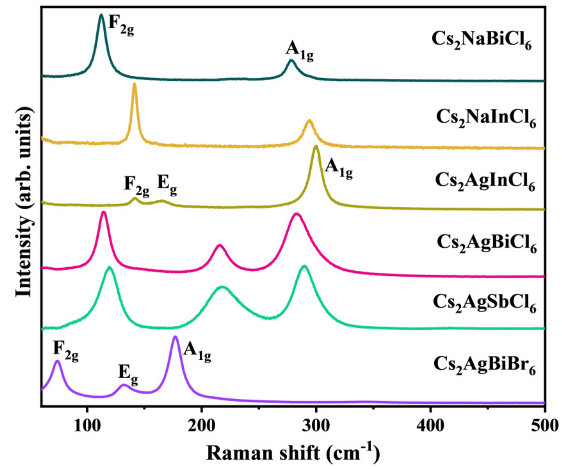

FIG. 8. Raman spectra of double perovskites with different cation and anion combinations.

We further analyzed the origin of asymmetric-stretching vibrations (i.e., E_g) by examining the Raman modes of double perovskites with different choices of B' and B'' cations and X anion. Figure 8 shows the Raman spectra of $Cs_2B'B''X_6$ double perovskites. The spectra reveal that the compounds with Ag^+ as B'-site cation shows asymmetric vibrations while the smaller Na^+ at B' site would exhibit only symmetric stretching. Whenever Ag^+ occupies B' site in the system, the cationic ordering decreases as inferred from XRD. Thus, antisite defects ($B'B''$ or $B''B'$) could result in a partially ordered system. This enhances the asymmetric vibrations in the octahedra. For the Na^+-based systems, the enhanced cationic ordering leads to a perfectly ordered structure and hence the asymmetric vibrations are significantly reduced. This is evident from the disappearance of E_g mode for Na^+-based double perovskites. This is consistent with the studies on some highly ordered perovskite oxides where the E_g mode appears to be very feeble or completely absent [40]. Also, a recent study by Singh *et al.* demonstrated that the intensity of asymmetric-stretching vibrations is susceptible to the strain in the crystal lattice [45]. Thus, it is clear from these analyses that the asymmetric-stretching mode can be a measure of sublattice distortions in the form of octahedral mismatch in double perovskite, and a highly ordered system would exhibit very minimal or no asymmetric vibrations.

IV. CONCLUSION

In summary, vibrational dynamics of $Cs_2B'B''X_6$ halide double perovskites have been investigated through comprehensive Raman spectral analyses. Structural analyses through XRD reveal solid-solution behavior and cationic ordering in double perovskites. The degree of cationic ordering increases with Na^+ substitution at Ag^+ site in $Cs_2Ag_{1-x}Na_xBiCl_6$ and $Cs_2Ag_{1-x}Na_xInCl_6$. Raman spectral studies further confirm this fact as we observe a significant enhancement in the F_{2g} mode intensities, a decrease in the linewidth of A_{1g} mode, and the disappearance of asymmetric-stretching vibrations (E_g mode) with Na^+ substitution. Further, careful analyses of Raman spectra obtained for a series of B' and B'' cation-substituted double perovskites disseminate the individual octahedral contributions for observed vibrational modes. Despite the fact that the octahedral framework is three-dimensionally connected, we find the octahedra with B'-site cation mainly influence the structural ordering and the vibrational intensities, while the B''-X_6 octahedra govern the energies of lattice vibrations. Besides, these results ascertain the origin of asymmetric-stretching vibrations in halide double perovskites. This could pave the way for tailoring the carrier-phonon interactions and optoelectronic properties by merely analyzing the vibrational modes of octahedra through Raman spectroscopy.

ACKNOWLEDGMENTS

C.S. acknowledges the support by DST-SERB for funding this work through Core Research Grants No. No. CRG/2021/001805, and SUPRA Grant No. SPR/2021/000499. C.S. acknowledges the Ministry of Education, Government of India, for funding this work through Scheme for Transformational and Advanced Research in Sciences (STARS) Grant No. STARS/APR2019/NS/537/FS. C.S. acknowledges the support by MHRD, India, through the Institutes of Eminence (Grant No. SP20210777DRMHRDDIRIIT) for the research initiatives on establishing the prospective Centre for Advanced Microscopy and Materials (Grant No. SB20210844MMMHRD008277).

[1] T. Leijtens, K. Bush, R. Cheacharoen, R. Beal, A. Bowring, and M. D. McGehee, Towards enabling stable lead halide perovskite solar cells; interplay between structural, environmental, and thermal stability, J. Mater. Chem. A **5**, 11483 (2017).
[2] A. Walsh, Principles of chemical bonding and band gap engineering in hybrid organic–inorganic halide perovskites, J. Phys. Chem. C **119**, 5755 (2015).
[3] A. Urbina, The balance between efficiency, stability and environmental impacts in perovskite solar cells: A review, J. Phys.: Energy **2**, 022001 (2020).
[4] W.-J. Yin, T. Shi, and Y. Yan, Unique properties of halide perovskites as possible origins of the superior solar cell performance, Adv. Mater. **26**, 4653 (2014).
[5] Z. Xiao, Z. Song, and Y. Yan, From lead halide perovskites to lead-free metal halide perovskites and perovskite derivatives, Adv. Mater. **31**, 1803792 (2019).
[6] W.-J. Yin, T. Shi, and Y. Yan, Superior photovoltaic properties of lead halide perovskites: Insights from first-principles theory, J. Phys. Chem. C **119**, 5253 (2015).
[7] A. Wang, Y. Guo, F. Muhammad, and Z. Deng, Controlled synthesis of lead-free cesium tin halide perovskite cubic nanocages with high stability, Chem. Mater. **29**, 6493 (2017).
[8] M. Pitaro, E. K. Tekelenburg, S. Shao, and M. A. Loi, Tin halide perovskites: from fundamental properties to solar cells, Adv. Mater. **34**, 2105844 (2022).
[9] L. A. Muscarella and E. M. Hutter, Halide double-perovskite semiconductors beyond photovoltaics, ACS Energy Lett. **7**, 2128 (2022).
[10] S. Khalfin and Y. Bekenstein, Advances in lead-free double perovskite nanocrystals, engineering band-gaps and enhancing stability through composition tunability, Nanoscale **11**, 8665 (2019).
[11] J. Leveillee, G. Volonakis, and F. Giustino, Phonon-limited mobility and electron–phonon coupling in lead-free halide double perovskites, J. Phys. Chem. Lett. **12**, 4474 (2021).
[12] R. Kentsch, M. Scholz, J. Horn, D. Schlettwein, K. Oum, and T. Lenzer, Exciton dynamics and electron–phonon coupling affect the photovoltaic performance of the $Cs_2AgBiBr_6$ double perovskite, J. Phys. Chem. C **122**, 25940 (2018).
[13] J. A. Steele, P. Puech, M. Keshavarz, R. Yang, S. Banerjee, E. Debroye, C. W. Kim, H. Yuan, N. H. Heo, J. Vanacken *et al.*, Giant electron–phonon coupling and deep conduction band resonance in metal halide double perovskite, ACS Nano **12**, 8081 (2018).
[14] L. Zhang, Y. Fang, L. Sui, J. Yan, K. Wang, K. Yuan, W. L. Mao, and B. Zou, Tuning emission and electron–phonon coupling in lead-free halide double perovskite $Cs_2AgBiCl_6$ under pressure, ACS Energy Lett. **4**, 2975 (2019).
[15] G. A. Elbaz, W.-L. Ong, E. A. Doud, P. Kim, D. W. Paley, X. Roy, and J. A. Malen, Phonon speed, not scattering, differentiates thermal transport in lead halide perovskites, Nano Lett. **17**, 5734 (2017).
[16] D. Manna, J. Kangsabanik, T. K. Das, D. Das, A. Alam, and A. Yella, Lattice dynamics and electron–phonon coupling in lead-free $Cs_2AgIn_{1-x}Bi_xCl_6$ double perovskite nanocrystals, J. Phys. Chem. Lett. **11**, 2113 (2020).
[17] Y. Yang, J. P. Robbins, L. Ezeonu, Y. Ma, N. Sparta, X. Kong, S. Strauf, S. G. Podkolzin, and S. S. Lee, Probing lattice vibrations of stabilized $CsPbI_3$ polymorphs via low-frequency Raman spectroscopy, J. Mater. Chem. C **8**, 8896 (2020).
[18] P. Pistor, A. Ruiz, A. Cabot, and V. Izquierdo-Roca, Advanced Raman spectroscopy of methylammonium lead iodide: Development of a non-destructive characterisation methodology, Sci. Rep. **6**, 35973 (2016).
[19] Y. Guo, O. Yaffe, D. W. Paley, A. N. Beecher, T. D. Hull, G. Szpak, J. S. Owen, L. E. Brus, and M. A. Pimenta, Interplay between organic cations and inorganic framework and incommensurability in hybrid lead-halide perovskite $CH_3NH_3PbBr_3$, Phys. Rev. Mater. **1**, 042401(R) (2017).

[20] A. C. Dakshinamurthy and C. Sudakar, Photoinduced degradation of thermally stable $Cs_2AgBiBr_6$ double perovskites by micro-Raman studies, Mater. Adv. **3**, 5813 (2022).

[21] M. A. Pérez-Osorio, Q. Lin, R. T. Phillips, R. L. Milot, L. M. Herz, M. B. Johnston, and F. Giustino, Raman spectrum of the organic–inorganic halide perovskite $CH_3NH_3PbI_3$ from first principles and high-resolution low-temperature Raman measurements, J. Phys. Chem. C **122**, 21703 (2018).

[22] A. C. Dakshinamurthy and C. Sudakar, Bandgap engineering and sublattice distortion driven bandgap bowing in $Cs_2Ag_{1-x}Na_xBiCl_6$ double perovskites, Appl. Phys. Lett. **118**, 131902 (2021).

[23] A. C. Dakshinamurthy and C. Sudakar, Sublattice distortion enabled strong interplay between phonon vibrations, electron–phonon coupling, and self-trapped excitonic emissions in $Cs_2Ag_{1-x}Na_xBiCl_6$ double perovskites, J. Phys. Chem. Lett. **13**, 433 (2022).

[24] D. Spirito, Y. Asensio, L. E. Hueso, and B. Martín-García, Raman spectroscopy in layered hybrid organic-inorganic metal halide perovskites, J. Phys. Mater. **5**, 034004 (2022).

[25] G. King and P. M. Woodward, Cation ordering in perovskites, J. Mater. Chem. **20**, 5785 (2010).

[26] K. D. Truong, J. Laverdière, M. P. Singh, S. Jandl, and P. Fournier, Impact of Co/Mn cation ordering on phonon anomalies in La_2CoMnO_6 double perovskites: Raman spectroscopy, Phys. Rev. B **76**, 132413 (2007).

[27] D. Sri Gyan, V. Sundram, A. Dwivedi, S. Bhowmick, and T. Maiti, Effect of B-site cation ordering on high temperature thermoelectric behavior of $Ba_xSr_{2-x}TiFeO_6$ double perovskites, J. Phys.: Condens. Matter **32**, 235401 (2020).

[28] P. Ksoll, C. Meyer, L. Schüler, V. Roddatis, and V. Moshnyaga, B-site cation ordering in films, superlattices, and layer-by-layer-grown double perovskites, Crystals **11**(7), 734 (2021).

[29] S. Vasala and M. Karppinen, $A_2B'B''O_6$ perovskites: A review, Prog. Solid State Chem. **43**, 1 (2015).

[30] See Supplemental Material at http://link.aps.org/supplemental/10.1103/PhysRevMaterials.7.065401 for raw XRD plots, EDS spectra with compositional details, magnified plot for x = 0.5 in $Cs_2NaBi_{1-x}In_xCl_6$, Raman spectra at various excitation energies and excitation powers.

[31] D. Rout, G. Santosh Babu, V. Subramanian, and V. Sivasubramanian, Study of cation ordering in $Ba(Yb_{1/2}Ta_{1/2})O_3$ by X-ray diffraction and Raman spectroscopy, Int. J. Appl. Ceram. Technol. **5**, 522 (2008).

[32] M. C. Knapp and P. M. Woodward, A-site cation ordering in $AA'BB'O_6$ perovskites, J. Solid State Chem. **179**, 1076 (2006).

[33] W. Yuan, G. Niu, Y. Xian, H. Wu, H. Wang, H. Yin, P. Liu, W. Li, and J. Fan, In situ regulating the order–disorder phase transition in $Cs_2AgBiBr_6$ single crystal toward the application in an x-ray detector, Adv. Funct. Mater. **29**, 1900234 (2019).

[34] J. Zhou, X. Rong, P. Zhang, M. S. Molokeev, P. Wei, Q. Liu, X. Zhang, and Z. Xia, Manipulation of Bi^{3+}/In^{3+} transmutation and Mn^{2+}-doping effect on the structure and optical properties of double perovskite $Cs_2NaBi_{1-x}In_xCl_6$, Adv. Opt. Mater. **7**, 1801435 (2019).

[35] A. C. Dakshinamurthy, M. Gupta, B. R. K. Nanda, and C. Sudakar, Anionic alloying in hybrid halide $Cs_2AgBiBr_{6-x}Cl_x$ double perovskites: Is it true alloying or preferential occupation of halide ions in MX_6 octahedra?, J. Phys. Chem. C **127**, 1588 (2023).

[36] A. Bhui, T. Ghosh, K. Pal, K. Singh Rana, K. Kundu, A. Soni, and K. Biswas, Intrinsically low thermal conductivity in the n-type vacancy-ordered double perovskite Cs_2SnI_6: Octahedral rotation and anharmonic rattling, Chem. Mater. **34**, 3301 (2022).

[37] A. Hossain, S. Roy, and K. Sakthipandi, The external and internal influences on the tuning of the properties of perovskites: An overview, Ceram. Int. **45**, 4152 (2019).

[38] J. Zhou, X. Rong, M. S. Molokeev, X. Zhang, and Z. Xia, Exploring the transposition effects on the electronic and optical properties of $Cs_2AgSbCl_6$ via a combined computational-experimental approach, J. Mater. Chem. A **6**, 2346 (2018).

[39] A. P. Ayala, I. Guedes, E. N. Silva, M. S. Augsburger, M. del C. Viola, and J. C. Pedregosa, Raman investigation of A_2CoBO_6 (A = Sr and Ca, B = Te and W) double perovskites, J. Appl. Phys. **101**, 123511 (2007).

[40] R. L. Andrews, A. M. Heyns, and P. M. Woodward, Raman studies of A_2MWO_6 tungstate double perovskites, Dalton Trans. **44**, 10700 (2015).

[41] L. Wang, W. Zheng, F. Vitale, X. Zhang, X. Li, Y. Ji, Z. Liu, O. Ghaebi, C. T. Plass, R. Domes *et al.*, Wide-bandgap double perovskites with multiple longitudinal-optical phonon scattering, Adv. Funct. Mater. **32**, 2111338 (2022).

[42] H. Zheng, I. M. Reaney, G. D. C. Csete de Györgyfalva, R. Ubic, J. Yarwood, M. P. Seabra, and V. M. Ferreira, Raman spectroscopy of $CaTiO_3$−based perovskite solid solutions, J. Mater. Res. **19**, 488 (2004).

[43] Y. Fujioka, J. Frantti, and M. Kakihana, Raman scattering studies of the Ba_2MnWO_6 and Sr_2MnWO_6 double perovskites, J. Phys. Chem. B **110**, 777 (2006).

[44] H. Siddique, Z. Xu, X. Li, S. Saeed, W. Liang, X. Wang, C. Gao, R. Dai, Z. Wang, and Z. Zhang, Anomalous octahedron distortion of bi-alloyed $Cs_2AgInCl_6$ crystal via XRD, Raman, Huang–Rhys factor, and photoluminescence, J. Phys. Chem. Lett. **11**, 9572 (2020).

[45] J. E. F. S. Rodrigues, C. A. Escanhoela, Jr., B. Fragoso, G. Sombrio, M. M. Ferrer, C. Álvarez-Galván, M. T. Fernández-Díaz, J. A. Souza, F. F. Ferreira, C. Pecharromán, and J. A. Alonso, Experimental and theoretical investigations on the structural, electronic, and vibrational properties of $Cs_2AgSbCl_6$ double perovskite, Ind. Eng. Chem. Res. **60**, 18918 (2021).

[46] M. N. Iliev, M. V. Abrashev, A. P. Litvinchuk, V. G. Hadjiev, H. Guo, and A. Gupta, Raman spectroscopy of ordered double perovskite La_2CoMnO_6 thin films, Phys. Rev. B **75**, 104118 (2007).

[47] M. Liegeois-Duyckaerts and P. Tarte, Vibrational studies of molybdates, tungstates and related c compounds—III. Ordered cubic perovskites $A_2B^{II}B^{VI}O_6$, Spectrochim. Acta Part A: Mol. Spectrosc. **30**, 1771 (1974).

[48] J. E. Rodrigues, D. M. Bezerra, and A. C. Hernandes, Calculation of the optical phonons in ordered Ba_2MgWO_6 perovskite using short-range force field model, J. Raman Spectrosc. **49**, 1822 (2018).

[49] J. Su, Z. Zhang, J. Hou, M. Liu, Z. Lin, Z. Hu, J. Chang, and Y. Hao, Pressure-dependent mechanical and thermal properties of lead-free halide double perovskite $Cs_2AgB''X_6$ (B″ = In, Bi; X = Cl, Br, I), Adv. Theory Simul. **2**, 1900164 (2019).

[50] K.-X. Xu, J.-M. Lai, Y.-F. Gao, F. Song, Y.-J. Sun, P.-H. Tan, and J. Zhang, High-order Raman scattering mediated by self-trapped exciton in halide double perovskite, Phys. Rev. B **106**, 085205 (2022).

[51] B. Zhang, J. Klarbring, F. Ji, S. I. Simak, I. A. Abrikosov, F. Gao, G. Y. Rudko, W. M. Chen, and I. A. Buyanova, Lattice dynamics and electron–phonon coupling in double perovskite $Cs_2NaFeCl_6$, J. Phys. Chem. C **127**, 1908 (2023).

[52] T. Appadurai, R. Kashikar, P. Sikarwar, S. Antharjanam, B. R. K. Nanda, and A. K. Chandiran, Manipulation of parity and polarization through structural distortion in light-emitting halide double perovskites, Commun. Mater. **2**, 68 (2021).

[53] F. Locardi, E. Sartori, J. Buha, J. Zito, M. Prato, V. Pinchetti, M. L. Zaffalon, M. Ferretti, S. Brovelli, I. Infante *et al.*, Emissive bi-doped double perovskite $Cs_2Ag_{1-x}Na_xInCl_6$ nanocrystals, ACS Energy Lett. **4**, 1976 (2019).

[54] K. Dave, W.-T. Huang, T. Leśniewski, A. Lazarowska, D. Jankowski, S. Mahlik, and R.-S. Liu, Photoluminescence enhancement study in a Bi-doped $Cs_2AgInCl_6$ double perovskite by pressure and temperature-dependent self-trapped exciton emission, Dalton Trans. **51**, 2026 (2022).

[55] T. Runka, R. Aleksiyko, M. Berkowski, and M. Drozdowski, Raman scattering study of $(SrAl_{0.5}Ta_{0.5}O_3)_{1\text{-x-y}}$: $(LaAlO_3)_x$: $(CaAl_{0.5}Ta_{0.5}O_3)_y$ solid solution crystals, Cryst. Res. Technol. **40**, 453 (2005).